RSC Advances

PAPER

View Article Online
View Journal | View Issue

Cite this: *RSC Adv.*, 2022, **12**, 11732

Improved hydrogen evolution performance by engineering bimetallic AuPd loaded on amino and nitrogen functionalized mesoporous hollow carbon spheres†

Lenan Wang,[ab] Zhankui Zhao,[a] Hongli Wang *[a] and Yue Chi *[ab]

Received 22nd February 2022
Accepted 7th April 2022

DOI: 10.1039/d2ra01191c

rsc.li/rsc-advances

A highly efficient heterogeneous catalyst was synthesized by delicate engineering of NH_2-functionalized and N-doped hollow mesoporous carbon spheres (NH_2–N-HMCS), which was used for supporting AuPd alloy nanoparticles with ultrafine size and good dispersion (denoted as AuPd/NH_2–N-HMCS). Without using any additives, the prepared AuPd/NH_2–N-HMCS catalytic formic acid dehydrogenation possesses superior catalytic activity with an initial turnover frequency value of 7747 mol H_2 per mol catalyst per h at 298 K. The excellent performance of AuPd/NH_2–N-HMCS derives from the unique hollow mesoporous structure, the small particle sizes and high dispersion of AuPd nanoparticles and the modified Pd electronic structure in the AuPd/NH_2–N-HMCS composite, as well as the synergistic effect of the modified support.

Introduction

With the rapid development of nanotechnology and catalysis science, metal nanoparticle catalysts have been widely used in industry and the laboratory.[1] Recently, considerable progress has revealed that Pd, Au, and their bimetallic nanomaterials are the most active catalysts for dehydrogenation of formic acid (HCOOH, FA),[2–4] which is a safe and convenient H_2 carrier with high volumetric H_2 density (53 g L^{-1}).[2] Pd alloying with Au can tune the surface electronic and geometric effects to optimize the catalysis, thus the bimetallic AuPd usually exhibits enhanced catalytic performance.[5,6] Although AuPd catalysis can enable the dehydrogenation of FA to proceed at milder conditions and with lower molar amounts of metal components, the reported catalytic performance is still far from being satisfactory even with assistance of additional additives.[3]

The introduction of catalyst supports with delicately designed nanostructures has constituted a reasonable strategy in improving the performance of metal catalysts. An appropriate support material not only acts as a physical carrier to disperse and stabilize the active metal, but interacts with the supported metal thus boosting the catalytic activity.[7] Up to now, the performance of supported metal catalysts can be enhanced by using different support materials, such as titanium dioxide,[8] zeolite,[9,10] porous carbon[11] and graphene oxide.[12] Among various supported metal catalysts, carbon-supported metal catalysts have recently attracted particular research interest, owing to the carbon frame employed as a substrate for growing supported metal, which also substantially influence the properties of supported metals through electronic interaction.[7] Particularly, hollow mesoporous carbon spheres (HMCS) would be attractive as catalyst supports for H_2 evolution from FA dehydrogenation comparing to conventional carbon supports. Such a structure provides a large void space, where reactants can freely diffuse in the cavity through mesoporous channels to participate in reaction.[13] The mesoporous shell not only induces the "confinement effect" to limit the growth and aggregation of supported metal, but also confines and enriches the reactants around the supported metal, leading to a locally increased reactant concentration and accelerating catalytic reaction.[13,14]

Unfortunately, the electronic interaction is usually weak between supported metal and a dopant-free carbon support, resulting in the aggregation of metal nanoparticles and the degradation of catalytic performance.[15] Introduction of heteroatom nitrogen brings more active π electrons to the carbon surface, which can not only *in situ* anchor the active metal nanoparticles, but also achieve the fine modulation of electronic structure of metal particles and maximize the strong metal-to-support interaction and thus enhance the catalytic performance.[16–18] However, N-doped hollow mesoporous carbon spheres (N-HMCS) can afford very limited application in FA system, as its nonpolar nature forces its tendency to aggregate and stack in aqueous solution, and unfavorable to adsorb

[a]*College of Material Science and Engineering, Key Laboratory of Advanced Structural Materials, Ministry of Education, Changchun University of Technology, Changchun, 130012, China. E-mail: yuechi@ccut.edu.cn; wanghongli@ccut.edu.cn*

[b]*Advanced Institute of Materials Science, Changchun University of Technology, Changchun, 130012, China*

† Electronic supplementary information (ESI) available. See https://doi.org/10.1039/d2ra01191c

polarity-featured reactants. To get enhanced catalytic performance, a further step beyond the preparation of N-HMCS is to introduce polar groups, such as $-NH_2$, which can endow the N-HMCS with hydrophilicity as well as impede aggregation of supported metal.[19] Furthermore, the $-NH_2$ groups can accelerate the cleavage of O–H bond in FA, thus accelerate the process of FA dehydrogenation and greatly improve the H_2 evolution activity of catalyst.[20,21]

In this work, we prepared NH_2-functionalized and N-doped hollow mesoporous carbon sphere (NH_2–N-HMCS) as a novel support for AuPd nanoparticles, and the resultant AuPd/NH_2–N-HMCS was used as catalyst for H_2 evolution from FA dehydrogenation. Benefitting from its spherical morphology, large cavity, high surface area, rich mesoporous structure, well-designed surface chemistry properties, metal–support interactions and synergistic catalysis of AuPd alloy nanoparticles, the AuPd/NH_2–N-HMCS exhibits excellent catalytic activity (up to 7747 mol H_2 per mol catalyst per h) and stability at room temperature without any additives.

Experimental

Materials

Resorcinol (Xilong Science Co., Ltd, ≥99.5%), formaldehyde (Sinopharm Chemical Reagent Co., Ltd, 37.0%), tetrapropyl orthosilicate (TPOS, Shanghai Mackin Biochemical Co., Ltd, 97%), ammonia solution ($NH_3 \cdot H_2O$, Beijing Chemical Works, 25–28%), hydrofluoric acid (HF, Sinopharm Chemical Reagent Co., Ltd, ≥40%), sulfuric acid (H_2SO_4, Beijing Chemical Works, 95–98%), ammonium persulfate (APS, Tianjin Xinbote Chemical Co., Ltd, ≥98%), 3-aminopropyl trimethoxysilane (APTMS, Aladdin Chemistry Co., Ltd, 97%), palladium chloride ($PdCl_2$, Sinopharm Chemical Reagent Co., Ltd, ≥59%), sodium chloride (NaCl, Sinopharm Chemical Reagent Co., Ltd, ≥99.5%), tetrachloroauric(III) acid ($HAuCl_4 \cdot 4H_2O$, Sinopharm Chemical Reagent Co., Ltd, Au > 47.8%), sodium borohydride ($NaBH_4$, Sinopharm Chemical Reagent Co., Ltd, ≥96%), formic acid (HCOOH, FA, Aladdin Chemistry Co., Ltd, ≥96%) and ethanol (CH_3CH_2OH, Tianjin Xinbote Chemical Co., Ltd, ≥99.7%) were used as received without further purification. High purified water from a Millipore Milli-Q water purification system was used in all the experiments.

Preparation of catalyst

HMCS were synthesized by a previously reported the one-pot and surfactant-free approach.[22,23] Firstly, 3.4 mL of TPOS was added into the mixed solution, which consisted of 70 mL ethanol, 10 mL distilled water and 3 mL ammonia, and stirred at 298 K for 15 minutes. Then, 0.4 g resorcinol and 0.5 mL formaldehyde were added to the solution in turn, and the stirring was continued for 24 h. The product was collected by centrifugation and washed six times alternately with water and ethanol, and dried at 323 K for 24 h. The dried specimen was calcined at 973 K under argon atmosphere for 5 h in a tubular furnace. Finally, the black products were desiliconized by hydrofluoric acid (5%) under strong magnetic stirring at room temperature for 24 h, and the reaction was repeated twice. The final product was washed with water and dried at 323 K for 12 h and denoted as HMCS.

Subsequently, 200 mg HMCS powder was evenly dispersed into 5 mL APS and H_2SO_4 mixed solution, and stirred at 298 K for 18 h. The concentrations of APS and H_2SO_4 in the solution were 1.7 M and 2 M respectively. The precipitates were centrifuged and washed with distilled water for 6 times. After drying at 373 K for 4 h, the surface oxidized mesoporous carbon hollow spheres were obtained and named as HMCS-O. Then, 0.2 mL APTMS was added into the pre ultrasonic HMCS-O aqueous solution (1.25 mg mL^{-1}, 35 mL), the $-NH_2$ functionalized and N-doped hollow mesoporous carbon spheres (NH_2–N-HMCS) were obtained after 10 min of ultrasonic treatment at 298 K.

AuPd nanoparticles were then introduced *via* impregnation reduction. Typically, for preparation of $Au_{0.3}Pd_{0.7}/NH_2$–N-HMCS, 2.5 mmol NaCl and 1.25 mmol $PdCl_2$ were put into 50.0 mL H_2O and stirred magnetically for 10 h to obtain Na_2PdCl_4 (0.025 M) solution. The $HAuCl_4 \cdot 4H_2O$ (0.02 M, 1.5 mL) and Na_2PdCl_4 (0.025 M, 2.8 mL) solution were added to the NH_2–N-HMCS aqueous solution with magnetic stirring at 298 K for 3 h. And then, $NaBH_4$ (40.5 mg) was added into the above mixed solution and stirred for 30 min. Finally, the resultant $Au_{0.3}Pd_{0.7}/NH_2$–N-HMCS product was separated and washed with water for several times.

In order to study the effect of different molar ratios of Au and Pd on dehydrogenation of formic acid, Au_xPd_{1-x}/NH_2–N-HMCS [$x = 0$, 0.1, 0.3, 0.5, 0.7, 0.9 and 1.0 calculated from the equation of $x = n_{Au}/(n_{Au} + n_{Pd})$] were synthesized in the similar method without changing the total molar weight of AuPd particles. For comparison, $Au_{0.3}Pd_{0.7}$/HMCS (the non-modified support material) and $Au_{0.3}Pd_{0.7}$ nanoparticles without any support were synthesized.

For comparison, $Au_{0.3}Pd_{0.7}$/N-HMCS was synthesized. Firstly, 100 mg HMCS was added into 10 mL ultrapure water and sonicated for 10 min. Then, 70 mL $NH_3 \cdot H_2O$ was poured into the mixture. Finally, the mixture was transferred to a Teflon-lined autoclave and heated at 473 K for 12 h to get N-HMCS. The N-HMCS were collected by centrifugation (10 000 rpm, 3 min) and washed repeatedly with ultrapure water and ethanol and dried at 333 K for 12 h. In order to introduce AuPd nanoparticles, 40 mg of N-HMCS was added into 35 mL H_2O for 10 min of ultrasonic treatment, then the $HAuCl_4 \cdot 4H_2O$ (0.02 M, 1.5 mL) and Na_2PdCl_4 (0.025 M, 2.8 mL) solution were added to the mixed solution with 3 h of magnetic stirring at 298 K. Finally, $NaBH_4$ (40.5 mg) was added as the reducing agent to obtain the $Au_{0.3}Pd_{0.7}$/N-HMCS product, the product was centrifuged and washed several times with distilled water.

Characterization

X-ray diffraction (XRD) patterns were collected using a Rigaku D/max 2500 vpc X-ray diffractometer operating at 40 kV and 100 mA with Cu Kα X-ray source. Field-emission scanning electron microscopy (FESEM) images were acquired on Zeiss model Gemini Supra 40 field emission scanning electron microscope. The transmission electron microscope (TEM), energy-dispersive

X-ray spectroscopy (EDS) and high-resolution transmission electron microscopy (HRTEM) images were obtained with an FEI-Talos-F200S microscope. The surface chemical properties of the specimens were measured using Fourier transform infrared spectrum (FTIR, Bio-Rad, FTS 6000). The nitrogen adsorption and desorption isotherms were measured at 77 K on a Micromeritics ASAP 2020 plus HD88 instrument (Micromeritics Instrument Corp, Norcross, GA). The Brunauer–Emmett–Teller (BET) specific surface area was calculated using desorption data. The pore size distribution curves were calculated based on the analysis of the desorption branch of the isotherm using the Barrett–Joyner–Halenda (BJH) algorithm. The Au and Pd content in the specimens were measured by inductively coupled plasma-optical emission spectroscopy (ICP-OES, Thermo Jarrell Ash (TJA) Atom scan Advantage). X-rays photoelectron spectroscopy (XPS) were acquired with an ESCALABMKLL (Vacuum Generators) spectrometer using Al Kα X-rays.

Catalytic activities

The as-prepared catalyst was put into a double neck round-bottom flask, one neck was connected to a gas burette, the other neck was connected to a pressure-equalizing funnel which contained FA solution (1 M, 5 mL). The reaction took place when the FA solution was added into the flask under magnetic stirring at 298 K. The gases generated were monitored by the gas burette, and the catalytic tests were carried out under the same conditions.

In order to investigate the stability of the catalyst, the cyclic catalytic experiments were carried out without changing the temperature and stirring speed. After the first catalytic reaction of $Au_{0.3}Pd_{0.7}/NH_2$–N-HMCS was thoroughly completed, an equivalent amount of FA aqueous solution (1 M, 5 mL) was injected into the flask to produce H_2 under magnetic stirring. The generation of gas was monitored by the gas burette.

TOF calculation

The initial TOF was calculated using the following equation:

$$\mathrm{TOF} = \frac{P_{\mathrm{atm}} V_{\mathrm{H_2}} / RT}{n_{\mathrm{catalyst}} t}$$

where P_{atm} is the atmospheric pressure, $V_{\mathrm{H_2}}$ is the volume of the generated H_2 when the conversion reaches 20%, R is the universal gas constant, T is the room temperature (298 K), n_{catalyst} is the measured amount of AuPd catalyst using ICP-OES, and t is the reaction time when the conversion reaches 20%.

Results and discussion

Preparation and characterization of catalysts

A multi-step process was used to synthesize AuPd/NH_2–N-HMCS. First, the HMCS was prepared through an *in situ* free assembly method, where the SiO_2@RF core–shell structure material was achieved by employing TPOS as the silica source for SiO_2 particles and resorcinol and formaldehyde as carbon sources. After pyrolysis to carbonize the organics and etching in HF to remove the SiO_2 template, the hollow structured HMCSs were obtained. The HMCS was blended with a mixture of APS and H_2SO_4 solution, after which the surface of HMCS was equipped with oxy functional groups, forming oxidized HMCS (HMCS-O). Then APTMS was introduced into the surface oxidized HMCS aqueous solution by sonication stirring at 298 K, during this process the oxy functional groups (–COOH and –OH) on the HMCS-O condensed with the silicon hydroxyl groups generated by hydrolysis of APTMS to form surface amine groups, and reacted with amine groups of APTMS to generate amide and C–N bonds, leading to NH_2-functionalized and N-doped hollow mesoporous carbon sphere (NH_2–N-HMCS). And then a small amount solution of $HAuCl_4$ and Na_2PdCl_4 (with an Au : Pd molar ratio of 0.3 : 0.7) was added into the above mixed solution with magnetic stirring. Finally, $NaBH_4$ was dissolved into the above-mentioned system, and the $Au_{0.3}Pd_{0.7}/NH_2$–N-HMCS could be promptly obtained. AuPd/N-HMCS and AuPd/HMCS were also prepared for comparison. Besides, the molar ratio of Au : Pd in AuPd/NH_2–N-HMCS has been changed by several values (0 : 1, 0.1 : 0.9, 0.3 : 0.7, 0.5 : 0.5, 0.7 : 0.3, 0.9 : 0.1, 1 : 0).

As shown in Fig. S1,† the HMCS are uniform hollow spheres with a disordered mesoporous channeled-wall structure, which can serve as a reservoir for metal precursors. After surface modification and metal loading, the $Au_{0.3}Pd_{0.7}/NH_2$–N-HMCS perfectly retain the original structure of the HMCS (Fig. S2†). The corresponding EDX of $Au_{0.3}Pd_{0.7}/NH_2$–N-HMCS displays all elements of C, N, Au, Pd, O and Si (Fig. S3†), and the molar ratio of Au : Pd is quantitatively determined to be 0.2924 : 0.7076 by the ICP-OES, in good agreement with the designed ratio. The $Au_{0.3}Pd_{0.7}/NH_2$–N-HMCS exhibits porous hollow sphere morphology with an average diameter and wall thickness of 450 nm and 75 nm (Fig. S2†), respectively. Differently, the surface of $Au_{0.3}Pd_{0.7}/NH_2$–N-HMCS with metal nanoparticles loading becomes coarse (Fig. 1a). Fig. 1b clearly shows that ultrafine AuPd nanoparticles are uniformly dispersed on the support. The average size of AuPd nanoparticles is estimated to be 2.2 nm by random count in TEM. While in $Au_{0.3}Pd_{0.7}$/N-HMCS, not only the AuPd nanoparticles supported on N-HMCS are well dispersed, but a mixture of various large-sized AuPd nanoparticles can be observed. This difference verifies the strong interaction between AuPd nanoparticles and NH_2–N-HMCS support, proving that the NH_2-functionalized and N-doped hollow mesoporous carbon sphere we reported is more effective for encapsulation of highly dispersed and ultrafine AuPd nanoparticles. As revealed in Fig. 1c, the $Au_{0.3}Pd_{0.7}$ nanoparticles have shown a typical crystalline character. The lattice spacing of the nanoparticle is measured to be 0.234 nm. This value is between the lattice spacing of (111) crystal planes in cubic Au (0.235 nm) and Pd (0.224 nm), confirming the formation of AuPd alloy. The wide-angle XRD pattern of the $Au_{0.3}Pd_{0.7}/NH_2$–N-HMCS (Fig. 1d) shows a broad diffraction peak that is corresponding to (111) crystal plane and located between the diffraction peak of Au (JCPDS card no. 65-8601) and Pd (JCPDS card no. 65-2867), indicating that the $Au_{0.3}Pd_{0.7}$ nanoparticles in $Au_{0.3}Pd_{0.7}/NH_2$–N-HMCS are formed in alloy structure, which is well consistent with the HRTEM result.[24] Compared with the XRD patterns of $Au_{0.3}Pd_{0.7}$/N-HMCS and

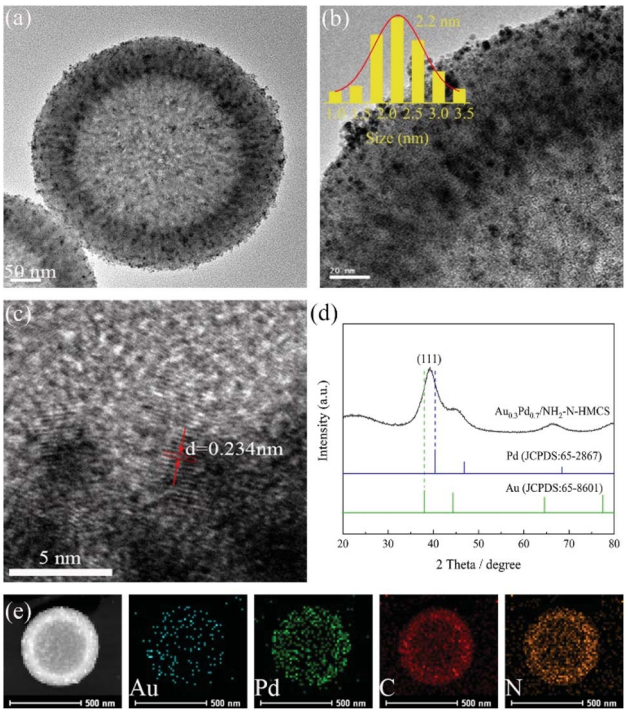

Fig. 1 TEM image and the size distribution of $Au_{0.3}Pd_{0.7}/NH_2$–N-HMCS (a and b), HRTEM image of $Au_{0.3}Pd_{0.7}/NH_2$–N-HMCS (c), XRD pattern of $Au_{0.3}Pd_{0.7}/NH_2$–N-HMCS (d), HAADF-STEM and the corresponding elemental mapping images of $Au_{0.3}Pd_{0.7}/NH_2$–N-HMCS (e).

$Au_{0.3}Pd_{0.7}$/HMCS (Fig. S4†), the peak of $Au_{0.3}Pd_{0.7}/NH_2$–N-HMCS centered around 39° is significantly broader, which further confirms the ultrafine size of $Au_{0.3}Pd_{0.7}$ nanoparticles in $Au_{0.3}Pd_{0.7}/NH_2$–N-HMCS. Fig. 1e shows the high-angle annular dark-field scanning transmission electron (HAADF-STEM) image and the corresponding Au, Pd, C and N EDX mapping images of $Au_{0.3}Pd_{0.7}/NH_2$–N-HMCS, where many isolated bright dots can be observed, demonstrating the presence of AuPd nanoparticles and their distribution on the NH_2–N-HMCS support. In addition, the elements of Au and Pd are co-distributed and homogenously dispersed on the positions of N and C elements, further evincing the uniform dispersion of AuPd nanoparticles in $Au_{0.3}Pd_{0.7}/NH_2$–N-HMCS.

The N_2 adsorption–desorption measurements of $Au_{0.3}Pd_{0.7}/NH_2$–N-HMCS exhibit a type IV adsorption isotherm similar to that of HMCS (Fig. 2), indicating the mesoporous structure has remained after surface modification and incorporation of AuPd nanoparticles. However, the surface area, pore size and total pore volume of $Au_{0.3}Pd_{0.7}/NH_2$–N-HMCS are calculated to be 593 $m^2\ g^{-1}$, 4.0 nm and 0.58 $cm^3\ g^{-1}$ respectively (Table 1), which significantly reduced compared to that of HMCS. According to previous studies,[25] loading metal in the pore channels would lead to remarkable perturbation of the pore size, surface area, and pore volume. Such phenomenon was also observed in this study, indicating the successful loading of AuPd nanoparticles in the mesoporous carbon support.

FTIR spectra were carried out to verify the functional groups of $Au_{0.3}Pd_{0.7}/NH_2$–N-HMCS (Fig. 3A). For HMCS, only one absorption at 1606 cm^{-1} corresponding to the aromatic C=C stretching vibration can be observed, indicating there is no other element or group modification on the HMCS. For HMCS-O, apart from the peak of C=C, it presents another three bands centered around 1719, 1401 and 1262 cm^{-1} that are not observed for the untreated HMCS.[26] A typical band at 1719 cm^{-1} assigned to –COOH groups is clearly visible, which suggests the carboxylic functional groups were successfully introduced upon surface oxidizing. In addition, the band at 1401 cm^{-1} can be assigned either to carboxyl–carbonate structure or aromatic C–C bonds whereas the band at 1262 cm^{-1} can be attributed to C–O–C vibrations in ether groups on the surface of HMCS-O. With APTMS treatment, several new absorption bands at 1203, 1111, 916 and 689 cm^{-1} were observed in the spectrum of $Au_{0.3}Pd_{0.7}/NH_2$–N-HMCS, related to N–H groups,[27] Si–O–C stretching vibration,[28] C–H bending vibration and C–N stretching vibration,[29,30] confirming the existence of $–NH_2$ groups and N doping in the NH_2–N-HMCS. Interestingly, compared with HMCS-O, the band at 1719 cm^{-1} is barely visible for $Au_{0.3}Pd_{0.7}/NH_2$–N-HMCS. The result further proves that the APTMS is grafted over the carboxylate groups on the surface of HMCS-O, through which the $–NH_2$ groups and N doping has been successfully introduced to the support. Moreover, the band centered at 680 cm^{-1} corresponding to C–N stretching vibration can be observed in the FTIR spectrum of $Au_{0.3}Pd_{0.7}/NH_2$–N-HMCS, proving that N element has been successfully doped in the support of this specimen.

To better understand surface composition and bonding environment of the prepared heterostructure, the $Au_{0.3}Pd_{0.7}/NH_2$–N-HMCS was studied by XPS analysis. Fig. S5† shows the fully scanned spectrum of $Au_{0.3}Pd_{0.7}/NH_2$–N-HMCS in the range of 0–1200 eV. The peaks on the curve of $Au_{0.3}Pd_{0.7}/NH_2$–N-HMCS are assigned to C, O, Au, Pd, Si and N elements, which is consistent with the EDX result. The electron structures of Pd and Au in the $Au_{0.3}Pd_{0.7}/NH_2$–N-HMCS catalyst were also analyzed by XPS, where the Pd 3d and Au 4f XPS spectra of $Au_{0.3}Pd_{0.7}/NH_2$–N-HMCS indicate that Pd and Au elements are mostly in metallic state, the minor portion of oxidized state of Pd(II) and Au(I) can be attributed to surface oxidation during sample preparation for XPS (Fig. 3B and S6†). Besides, the XPS results of Pd 3d in $Au_{0.3}Pd_{0.7}/NH_2$–N-HMCS, Pd/NH_2–N-HMCS and unsupported $Au_{0.3}Pd_{0.7}$ were also measured for comparison (Fig. 3B). Compared with the unsupported $Au_{0.3}Pd_{0.7}$, the Pd 3d peak in Pd/NH_2–N-HMCS shifted to a higher binding energy (from 335.5 to 335.8 eV), which can be attributed to the partial transfer of electrons from Pd to the NH_2–N-HMCS support caused by the strong interactions between metal and support.

In addition, the peaks of Pd 3d in $Au_{0.3}Pd_{0.7}/NH_2$–N-HMCS shifted toward lower binding energies in comparison with that of Pd/NH_2–N-HMCS (from 335.8 to 335.6 eV), indicating the electron structure of Pd can be adjusted by adding Au through electron synergetic effect, which further confirms the formation of alloy structure in AuPd nanoparticles. It is also noteworthy that in comparison with the unsupported $Au_{0.3}Pd_{0.7}$, both peaks

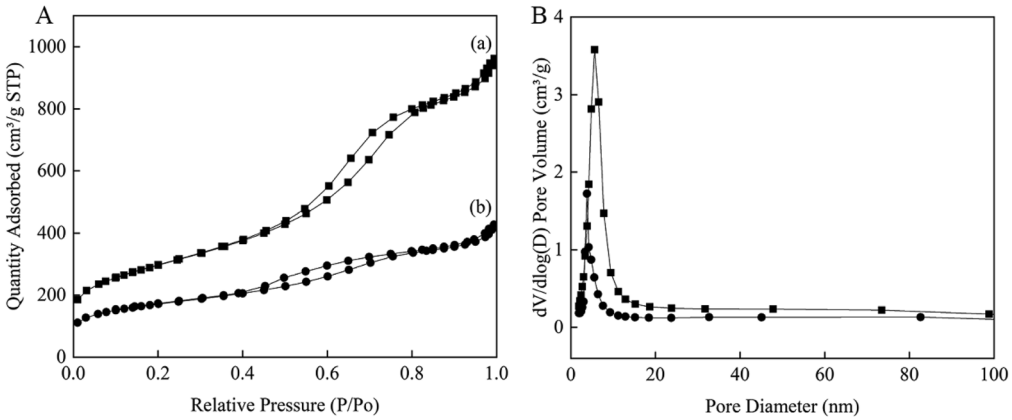

Fig. 2 Nitrogen adsorption–desorption isotherms (A) and the corresponding pore size distributions (B) of the samples of (a) HMCS and (b) $Au_{0.3}Pd_{0.7}/NH_2$–N-HMCS.

Table 1 Textural properties of HMCS and $Au_{0.3}Pd_{0.7}/NH_2$–N-HMCS

Sample	Pore size (nm)	BET surface area ($m^2\ g^{-1}$)	Pore volume ($cm^3\ g^{-1}$)
HMCS	5.2	1051	1.35
$Au_{0.3}Pd_{0.7}/NH_2$–N-HMCS	4.0	593	0.58

of Pd 3d in $Au_{0.3}Pd_{0.7}/NH_2$–N-HMCS shifted toward higher binding energies, owing to the metal–support interactions and electron synergetic effect. This shift reveals more electron depletion state of Pd in $Au_{0.3}Pd_{0.7}/NH_2$–N-HMCS, which can endow $Au_{0.3}Pd_{0.7}/NH_2$–N-HMCS with excellent catalytic activity for H_2 generation from FA as a result of the acceleration for C–H cleavage in the adsorbed formate.[31]

The high resolution XPS spectra confirm the chemical states of N in $Au_{0.3}Pd_{0.7}/NH_2$–N-HMCS and $Au_{0.3}Pd_{0.7}$/N-HMCS. As shown in Fig. 3C and D, the N 1s peaks of $Au_{0.3}Pd_{0.7}/NH_2$–N-HMCS and $Au_{0.3}Pd_{0.7}$/N-HMCS are centered at ≈398.7 and ≈400.1 eV, respectively, indicating different chemical states of N in the sample. The N 1s XPS spectrum of $Au_{0.3}Pd_{0.7}/NH_2$–N-HMCS can be fitted into three components with binding energy

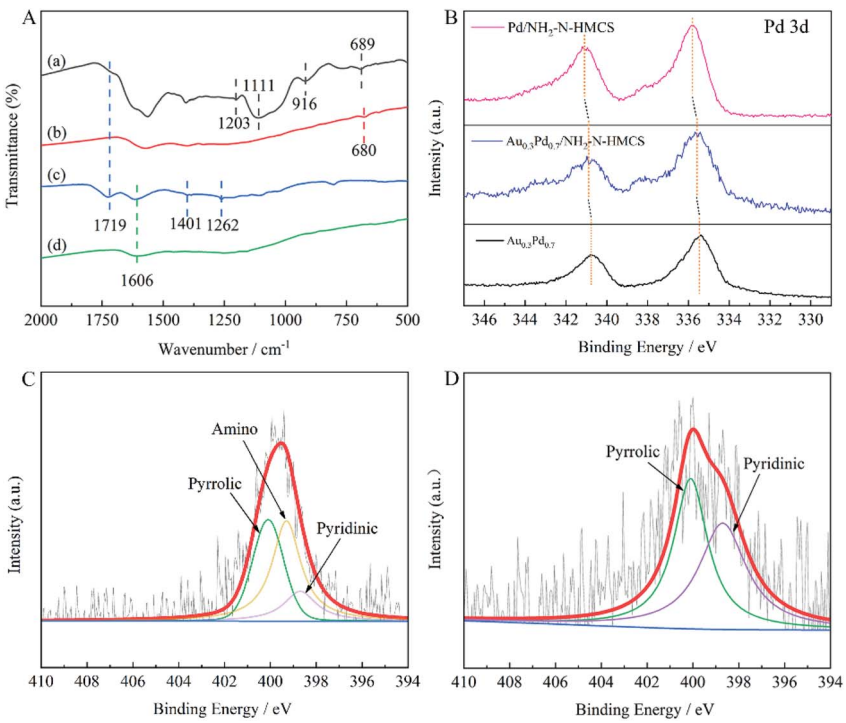

Fig. 3 (A) FTIR spectra of $Au_{0.3}Pd_{0.7}/NH_2$–N-HMCS (a), $Au_{0.3}Pd_{0.7}$/N-HMCS (b), HMCS-O (c) and HMCS (d), (B) the high-resolution XPS spectra of Pd 3d for Pd/NH_2–N-HMCS, $Au_{0.3}Pd_{0.7}/NH_2$–N-HMCS and $Au_{0.3}Pd_{0.7}$, (C) the high-resolution XPS spectrum of N 1s for $Au_{0.3}Pd_{0.7}/NH_2$–N-HMCS and (D) $Au_{0.3}Pd_{0.7}$/N-HMCS.

of 398.7, 399.3, 400.1 eV corresponding to the pyridinic N, amino N, and pyrrolic N, respectively, while that in $Au_{0.3}Pd_{0.7}$/N-HMCS can be assigned to pyridinic N (398.7 eV) and pyrrolic N (400.1 eV).[32,33] Taking both XPS and FTIR results into account, N in $Au_{0.3}Pd_{0.7}$/N-HMCS is proven to be the doping atoms, while N in $Au_{0.3}Pd_{0.7}/NH_2$–N-HMCS exists in forms of doping atoms and $-NH_2$ group.

Catalytic activity

The as-prepared $Au_{0.3}Pd_{0.7}/NH_2$–N-HMCS catalyst has excellent catalytic activity for H_2 generation from FA (1.0 M, 5 mL) without any additives at 298 K under ambient atmosphere (Fig. 4a). Obviously, the $Au_{0.3}Pd_{0.7}/NH_2$–N-HMCS exhibits the highest catalytic activity for FA decomposition among all the prepared catalysts, with which 224 mL of gas can be released within 67 s, corresponding 100% conversion. To understand the effect of different Au/Pd molar ratio on the dehydrogenation activity towards FA, various Au_xPd_{1-x}/NH_2–N-HMCS ($0 \leq x \leq 1.0$) with different Au : Pd molar ratios were synthesized and used for dehydrogenation of FA. As shown in Fig. S7,† the Au/NH_2–N-HMCS sample shows very low catalytic activity for FA, and the catalytic activities of nanocomposites containing AuPd binary alloy (AuPd/NH_2–N-HMCS) are higher than those containing single metal (Au/NH_2–N-HMCS and Pd/NH_2–N-HMCS).[34–37] This phenomenon can be attributed to the electron synergetic effect between Pd and Au, which has been proven by fore-mentioned XPS analysis. In addition, the molar ratio of Au to Pd has also been found to be critical in the catalytic dehydrogenation reaction. With the increase of the Au content, the catalytic activity of Au_xPd_{1-x}/NH_2–N-HMCS first increases, exhibiting the maximum initial turnover frequency (TOF) value of 7747 mol H_2 per mol catalyst per h at $x = 0.3$. However, the further increase in Au content results in a negative impact on the catalytic dehydrogenation reaction, which is due to the fact that Au does not have high catalytic activity toward FA. The excellent catalytic activity of the $Au_{0.3}Pd_{0.7}/NH_2$–N-HMCS results from the modulation of the electronic structure of Pd by introducing a proper amount of Au and the synergistic catalysis between the carrier and the metal.

To further understand the mechanism for the enhanced catalytic activity towards FA decomposition by $Au_{0.3}Pd_{0.7}/NH_2$–N-HMCS, the catalytic performance of unsupported $Au_{0.3}Pd_{0.7}$ nanoparticles, $Au_{0.3}Pd_{0.7}$/HMCS (without any functionalization), and $Au_{0.3}Pd_{0.7}$/N-HMCS in H_2 generation are given for comparison and reference (Fig. 4a), which clearly shows that the $Au_{0.3}Pd_{0.7}$ nanoparticles (50 mL, 53 min) and $Au_{0.3}Pd_{0.7}$/HMCS (20 mL, 10 min) have much lower catalytic activities. For $Au_{0.3}Pd_{0.7}$/HMCS, the HMCS without any functionalization cannot provide sufficient coordination sites to facilitate the formation of AuPd nanoparticles, thus resulting in the low particle dispersity (Fig. S8†) and finally causes severe degradation of catalytic performance. For $Au_{0.3}Pd_{0.7}$/N-HMCS, it can release 180 mL gas from FA within 23 min, giving an 80% conversion. The hollow morphology and interconnected mesopores of N-HMCS can facilitate mass diffusion and accessibility, which helps in improving the catalytic performance. In addition, the N-doped N-HMCS is conducive to the formation of highly dispersed $Au_{0.3}Pd_{0.7}$ nanoparticles (Fig. S9†), thus expose more active sites and enhance its catalytic performance. However, a few of large and agglomerated $Au_{0.3}Pd_{0.7}$ nanoparticles were also detected in the $Au_{0.3}Pd_{0.7}$/N-HMCS, which impedes their catalytic performance. All in all, the $Au_{0.3}Pd_{0.7}$/N-HMCS exhibits much lower catalytic activities compared with $Au_{0.3}Pd_{0.7}/NH_2$–N-HMCS. The significant enhancement on the catalytic performance of $Au_{0.3}Pd_{0.7}/NH_2$–N-HMCS can be ascribed to the introduction of amine groups that improve the wettability of the carbon materials and thus lead to the ultrafine particle sizes and good dispersion. Besides, it has been reported that amine groups in supported Pd-based catalysts can facilitate the FA adsorption and the cleavage of O–H bond in FA molecules, and thereby greatly improve the catalytic activities for H_2 evolution from FA dehydrogenation.[38,39] On top of that, the $Au_{0.3}Pd_{0.7}/NH_2$–N-HMCS has outstanding catalytic activity for heterogeneously catalyzed FA dehydrogenation ever reported without any additives,[3,17,33,40] and moreover, could be comparable to the most active catalysts with additives under elevated temperatures (Table S1†).[6,9,11,41]

The reusability of the catalysts $Au_{0.3}Pd_{0.7}/NH_2$–N-HMCS was also tested. The recycling stability of the $Au_{0.3}Pd_{0.7}/NH_2$–N-HMCS is evaluated by adding the same amount of the FA solution to the reaction vessel after completion of the previous run. There is a slight decay in catalytic activity after four cycles (Fig. S10†). The TEM image of the sample after the 4th run shows that the nanoparticles still maintain good dispersion with a slight increase in the particle size (from 2.2 to 2.7 nm; Fig. S11†), which maybe the reason for the decrease in catalytic activity. The above analysis indicates the good recycling stability of $Au_{0.3}Pd_{0.7}/NH_2$–N-HMCS towards FA dehydrogenation reaction.

Based on the comparative experimental investigations and results, a possible mechanism for $Au_{0.3}Pd_{0.7}/NH_2$–N-HMCS catalyzed FA dehydrogenation has been proposed (Fig. 5). After adsorption of FA molecules on $Au_{0.3}Pd_{0.7}/NH_2$–N-HMCS, the amine groups can donate electrons and act as a proton scavenger to promote O–H cleavage and produce H^+. Subsequently, $HCOO^-$ adsorbs on the surface of metal nanoparticles and forms the metal-formate intermediates. Then, the rate determining step is promoted by the Pd with more electron depletion state in $Au_{0.3}Pd_{0.7}/NH_2$–N-HMCS, which can

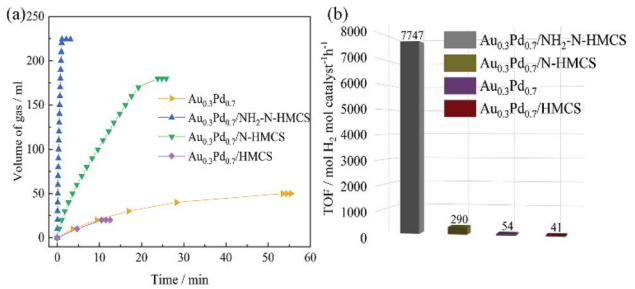

Fig. 4 Gas generation from the dehydrogenation of FA (1.0 M, 5.0 mL) *versus* time (a), initial TOF values of $Au_{0.3}Pd_{0.7}/NH_2$–N-HMCS, $Au_{0.3}Pd_{0.7}$/N-HMCS, $Au_{0.3}Pd_{0.7}$ and $Au_{0.3}Pd_{0.7}$/HMCS (b).

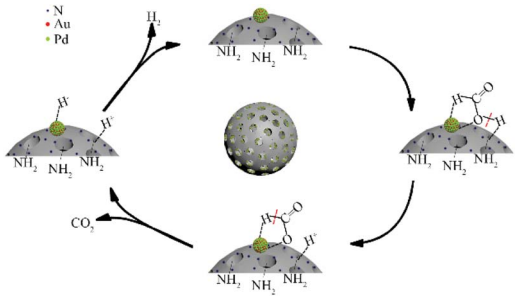

Fig. 5 Reaction pathway of the dehydrogenation of FA catalyzed by $Au_{0.3}Pd_{0.7}/NH_2$–N-HMCS.

accelerate C–H cleavage in the adsorbed formate to form H^- and release CO_2. Finally, the generated H^- combines with H^+ to produce H_2, along with the regeneration of active centers.[40,42] The excellent catalytic performance of this synthesized $Au_{0.3}Pd_{0.7}/NH_2$–N-HMCS nanocomposites can be ascribed to the following four factors. Firstly, the hollow morphology and interconnected mesopores can not only facilitate mass diffusion and accessibility but also confine and enrich the reactants around the supported metal, which helps in improving the catalytic performance. Secondly, NH_2-functionalized and N-doped support could effectively immobilize the metal ion by chemical complexation and favor the formation of highly dispersed and small sized metal nanoparticles. Thirdly, the $–NH_2$ group can act as a proton scavenger and facilitate the cleavage of O–H bond in FA molecules. Fourthly, the more electron depletion state of Pd in $Au_{0.3}Pd_{0.7}/NH_2$–N-HMCS caused by metal–support interactions and electron synergetic effect can accelerate the C–H cleavage in the adsorbed formate and the formation of H^-.[43–45]

Conclusions

In summary, a novel nanocomposite $Au_{0.3}Pd_{0.7}/NH_2$–N-HMCS has been designed and synthesized in this work, which shows highly efficient catalytic activity for hydrogen generation from aqueous solutions of formic acid, and affords an excellent TOF value as high as 7747 mol H_2 per mol catalyst per h at 298 K without any additives. The novel NH_2–N-HMCS substrate with spherical morphology, large surface area, sufficient pore volume, rich mesoporous structure, nitrogen doping and $–NH_2$ functionalized surface endows the *in situ* formed $Au_{0.3}Pd_{0.7}$ nanoparticles with ultrafine size (2.2 nm) and high dispersity, and the occurring of metal–support interactions and electron transfer between metals, which are the key factors responsible for the excellent catalytic activity of $Au_{0.3}Pd_{0.7}/NH_2$–N-HMCS. This work sheds light on designing highly efficient and durable heterogeneous catalysts through nanostructure engineering for promising applications towards formic acid as a hydrogen storage power source.

Conflicts of interest

There are no conflicts to declare.

Acknowledgements

This work was supported by the Science and Technology Research Project of the Education Department of Jilin Province (No. JJKH20210728KJ) and the National Natural Science Foundation of China (No. 51608050).

Notes and references

1 R. J. White, R. Luque, V. L. Budarin, J. H. Clark and D. J. Macquarrie, *Chem. Soc. Rev.*, 2009, **38**, 481–494.
2 Z. Li and Q. Xu, *Acc. Chem. Res.*, 2017, **50**, 1449–1458.
3 M. Wen, K. Mori, Y. Kuwahara and H. Yamashita, *ACS Energy Lett.*, 2017, **2**, 1–7.
4 Z. Wang, C. Wang, S. Mao, Y. Gong, Y. Chen and Y. Wang, *J. Mater. Chem. A*, 2019, **7**, 25791–25795.
5 Z. Wang, S. Liang, X. Meng, S. Mao, X. Lian and Y. Wang, *Appl. Catal., B*, 2021, **291**, 120140.
6 Q. Wang, L. Chen, Z. Liu, N. Tsumori, M. Kitta and Q. Xu, *Adv. Funct. Mater.*, 2019, **29**, 1903341.
7 M. Navlani-García, K. Mori, Y. Kuwahara and H. Yamashita, *NPG Asia Mater.*, 2018, **10**, 277–292.
8 Z. Zhang, S. Cao, Y. Liao and C. Xue, *Appl. Catal., B*, 2015, **162**, 204–209.
9 N. Wang, Q. Sun, R. Bai, X. Li, G. Guo and J. Yu, *J. Am. Chem. Soc.*, 2016, **138**, 7484–7487.
10 Q. Sun, B. W. J. Chen, N. Wang, Q. He, A. Chang, C. Yang, H. Asakura, T. Tanaka, M. J. Hülsey, C. Wang, J. Yu and N. Yan, *Angew. Chem., Int. Ed.*, 2020, **132**, 20358–20366.
11 J. Cheng, X. Gu, X. Sheng, P. Liu and H. Su, *J. Mater. Chem. A*, 2016, **4**, 1887–1894.
12 M. Khalid, X. Zarate, M. Saavedra-Torres, E. Schott, A. M. B. Honorato, M. R. Hatshan and H. Varela, *Chem. Eng. J.*, 2021, **421**, 129987.
13 G. Prieto, H. Tüysüz, N. Duyckaerts, J. Knossalla, G. H. Wang and F. Schüth, *Chem. Rev.*, 2016, **116**, 14056–14119.
14 Y. Li and J. Shi, *Adv. Mater.*, 2014, **26**, 3176–3205.
15 T. Fu, M. Wang, W. Cai, Y. Cui, F. Gao, L. Peng, W. Chen and W. Ding, *ACS Catal.*, 2014, **4**, 2536–2543.
16 Q. Wang, N. Tsumori, M. Kitta and Q. Xu, *ACS Catal.*, 2018, **8**, 12041–12045.
17 Q. Bi, J. Lin, Y. Liu, H. He, F. Huang and Y. Cao, *Angew. Chem., Int. Ed.*, 2016, **55**, 11849–11853.
18 H. Wang, T. Maiyalagan and X. Wang, *ACS Catal.*, 2012, **2**, 781–794.
19 J. Cheng, X. Gu, P. Liu, T. Wang and H. Su, *J. Mater. Chem. A*, 2016, **4**, 16645–16652.
20 H. Wang, Y. Chi, D. Gao, Z. Wang, C. Wang, L. Wang, M. Wang, D. Cheng, J. Zhang, C. Wu and Z. Zhao, *Appl. Catal., B*, 2019, **255**, 117776.
21 K. Mori, M. Dojo and H. Yamashita, *ACS Catal.*, 2013, **3**, 1114–1119.
22 H. Zhang, O. Noonan, X. Huang, Y. Yang, C. Xu, L. Zhou and C. Yu, *ACS Nano*, 2016, **10**, 4579–4586.
23 B. Shao, Z. Liu, G. Zeng, Y. Liu, X. Yang, C. Zhou, M. Chen, Y. Liu, Y. Jiang and M. Yan, *J. Hazard. Mater.*, 2019, **362**, 318–326.

24 W. Nie, Y. Luo, Q. Yang, G. Feng, Q. Yao and Z. Lu, *Inorg. Chem. Front.*, 2020, **7**, 709–717.
25 Y. Zhang, F. Jiang, D. Huang, S. Hou, H. Wang, M. Wang, Y. Chi and Z. Zhao, *RSC Adv.*, 2018, **8**, 31348–31357.
26 Y. Chi, L. Zhao, Q. Yuan, X. Yan, Y. Li, N. Li and X. Li, *J. Mater. Chem.*, 2012, **22**, 13571–13577.
27 V. Duraisamy and R. Krishnan, *ACS Appl. Nano Mater.*, 2020, **3**, 8875–8887.
28 M. Singh and S. Chauhan, *J. Appl. Polym. Sci.*, 2007, **104**, 3261–3268.
29 T. Gallardo-Velázquez, G. Osorio-Revilla, M. Zuñiga-deLoa and Y. Rivera-Espinoza, *Food Res. Int.*, 2009, **42**, 313–318.
30 Z. Lin, M. Song, Y. Ding, Y. Liu, M. Liu and C. Wong, *Phys. Chem. Chem. Phys.*, 2012, **14**, 3381–3387.
31 K. Tedsree, T. Li, S. Jones, C. W. A. Chan, K. M. K. Yu, P. A. J. Bagot, E. A. Marquis, G. D. W. Smith and S. C. E. Tsang, *Nat. Nanotechnol.*, 2011, **6**, 302–307.
32 C. Zhang, R. Hao, H. Liao and Y. Hou, *Nano Energy*, 2013, **2**, 88–97.
33 J. Yan, S. Li, S. Yi, B. R. Wulan, W. Zheng and Q. Jiang, *Adv. Mater.*, 2018, **30**, 1703038.
34 P. Liu, X. Gu, H. Zhang, J. Cheng, J. Song and H. Su, *Appl. Catal., B*, 2017, **204**, 497–504.
35 X. Yang, P. Pachfule, Y. Chen, N. Tsumori and Q. Xu, *Chem. Commun.*, 2016, **52**, 4171–4174.
36 L. Xu, F. Yao, J. Luo, C. Wan, M. Yea, P. Cui and Y. An, *RSC Adv.*, 2017, **7**, 4746–4752.
37 A. Al-Nayili and M. Albdiry, *New J. Chem.*, 2021, **45**, 10040–10048.
38 A. Bulut, M. Yurderi, Y. Karatas, Z. Say, H. Kivrak, M. Kaya, M. Gulcan, E. Ozensoy and M. Zahmakiran, *ACS Catal.*, 2015, **5**, 6099–6110.
39 Y. Karatas, A. Bulut, M. Yurderi, I. E. Ertas, O. Alal, M. Gulcan, M. Celebi, H. Kivrak, M. Kaya and M. Zahmakiran, *Appl. Catal., B*, 2016, **180**, 586–595.
40 J. Cheng, X. Gu, P. Liu, H. Zhang, L. Ma and H. Su, *Appl. Catal., B*, 2017, **218**, 460–469.
41 Y. Chen, Q. Zhu, N. Tsumori and Q. Xu, *J. Am. Chem. Soc.*, 2015, **137**, 106–109.
42 D. Gao, Z. Wang, C. Wang, L. Wang, Y. Chi, M. Wang, J. Zhang, C. Wu, Y. Gu and H. Wang, *Chem. Eng. J.*, 2019, **361**, 953–959.
43 L. Zhang, J. Zhu, X. Li, S. Mu, F. Verpoort, J. Xue, Z. Kou and J. Wang, *Interdiscip. Mater.*, 2022, **1**, 51–87.
44 T. Wang, P. Wang, W. Zang, X. Li, D. Chen, Z. Kou, S. Mu and J. Wang, *Adv. Funct. Mater.*, 2022, **32**, 2107382.
45 T. Wang, P. Wang, Y. Pang, Y. Wu, J. Yang, H. Chen, X. Gao, S. Mu and Z. Kou, *Nano Res.*, 2022, DOI: **10.1007/s12274-022-4072-5**.